

EXPERIMENTAL STUDIES ON THE FORMATION OF D₂O AND D₂O₂ BY IMPLANTATION OF ENERGETIC D⁺ IONS INTO OXYGEN ICES

CHRIS J. BENNETT^{1,2,3}, COURTNEY P. ENNIS^{1,4}, AND RALF I. KAISER^{1,2}

¹ Department of Chemistry, University of Hawai'i at Mānoa, Honolulu, HI 96822, USA; ralfk@hawaii.edu

² Institute for Astronomy and NASA Astrobiology Institute, 2680 Woodlawn Drive, University of Hawai'i, Honolulu, HI 96822, USA

Received 2013 July 25; accepted 2013 December 12; published 2014 January 28

ABSTRACT

The formation of water (H₂O) in the interstellar medium is intrinsically linked to grain-surface chemistry; thought to involve reactions between atomic (or molecular) hydrogen with atomic oxygen (O), molecular oxygen (O₂), and ozone (O₃). Laboratory precedent suggests that H₂O is produced efficiently when O₂ ices are exposed to H atoms (~100 K). This leads to the sequential generation of the hydroxyperoxyl radical (HO₂), then hydrogen peroxide (H₂O₂), and finally H₂O and a hydroxyl radical (OH); despite a barrier of ~2300 K for the last step. Recent detection of the four involved species toward ρ Oph A supports this general scenario; however, the precise formation mechanism remains undetermined. Here, solid O₂ ice held at 12 K is exposed to a monoenergetic beam of 5 keV D⁺ ions. Products formed during the irradiation period are monitored through FTIR spectroscopy. O₃ is observed through seven archetypal absorptions. Three additional bands found at 2583, 2707, and 1195 cm⁻¹ correspond to matrix isolated DO₂ (ν₁) and D₂O₂ (ν₁, ν₅), and D₂O (ν₂), respectively. During subsequent warming, the O₂ ice sublimates, revealing a broad band at 2472 cm⁻¹ characteristic of amorphous D₂O (ν₁, ν₃). Sublimating D₂, D₂O, D₂O₂, and O₃ products were confirmed through their subsequent detection via quadrupole mass spectrometry. Reaction schemes based on both thermally accessible and suprathermally induced chemistries were developed to fit the observed temporal profiles are used to elucidate possible reaction pathways for the formation of D₂-water. Several alternative schemes to the hydrogenation pathway (O₂→HO₂→H₂O₂→H₂O) were identified; their astrophysical implications are briefly discussed.

Key words: astrochemistry – cosmic rays – ISM: molecules – methods: laboratory: solid state – molecular processes – radiation mechanisms: non-thermal

Online-only material: color figures

1. INTRODUCTION

Gas-phase water (H₂O) and molecular oxygen (O₂) have both been detected within the interstellar medium (ISM). Over 40 yr ago, Cheung et al. (1969) monitored water toward Orion, Sgr B2, and W49 through its 22 GHz maser emission line. Confirmation of the presence of oxygen has remained elusive until recently. Larsson et al. (2007) used the Odin satellite to detect oxygen via its 119 GHz emission line toward ρ Oph A. Follow up observations by Goldsmith et al. (2011) using the *Herschel Space Observatory*, confirmed the presence of oxygen toward Orion via three separate lines at 487, 774, and 1121 GHz; indicating an upper fractional abundance of 7.3×10^{-6} , i.e., only about 1% of the total interstellar oxygen. The authors present an overview of the historic attempts to detect this species, which has been hindered not only by observational difficulties but also due to the low abundance of this species. Therefore, it has been suggested that condensation of molecular oxygen onto interstellar grains in cold molecular clouds might be responsible for the observed lack of gas-phase molecular oxygen (Du et al. 2012).

On the other hand, water ice was identified toward Orion through its 3.1 μm (~3226 cm⁻¹) absorption band by Gillett & Forrest (1973). Since this study, water has been found

to be consistently the most abundant species condensed on interstellar ices throughout spectral surveys conducted with both the *Infrared Space Observatory* (Gibb et al. 2004) and *Spitzer* (Boogert et al. 2008). The abundance of water ice is approximately up to three orders of magnitude higher than that predicted to be formed from gas-phase mechanisms, suggesting that it cannot be accounted for by the freeze-out of gas-phase water (Hasegawa et al. 1992; Bergin et al. 2000; Roberts & Herbst 2002). Considering that the abundance of molecular oxygen is lower than expected, molecular oxygen may be converted to water on interstellar grains (Du et al. 2012).

Tielens & Hagen (1982) produced the first astrochemical models incorporating grain-chemistry where the formation of water was thought to form via reactions of atomic hydrogen (H), or molecular hydrogen (H₂), with atomic oxygen (O) and molecular oxygen as well as ozone (O₃). Since then, multiple reaction pathways for water formation have been proposed on interstellar grains. The simplest mechanism is the stepwise and barrier-less addition of hydrogen atoms to atomic oxygen (reactions 1 and 2):



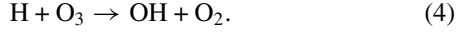
An alternative formation route via the reaction of molecular hydrogen with hydroxyl radicals (Equation (3)) was suggested to have a barrier of about 2100 K and hence thought to be much less efficient.



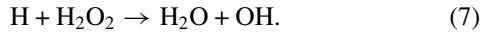
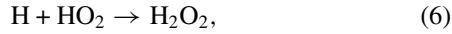
³ Current address: Chemistry & Biochemistry, Georgia Institute of Technology, 901 Atlantic Drive, Atlanta, GA 30332-0400, USA.

⁴ Current address: Department of Chemistry, University College London, 20 Gordon Street, London WC1H 0AJ, UK.

However, Cuppen & Herbst (2007) speculated that under certain conditions, this might be the most efficient pathway to water. If the hydroxyl radical reactant (OH) has sufficient internal energy, i.e., in a vibrationally excited state, the entrance barrier to reaction with molecular hydrogen can be reduced substantially. Here, vibrationally excited hydroxyl radicals might be formed on grains via the reaction of ozone with atomic hydrogen (reaction 4; Fernández-Ramos & Varandas 2002), leading to the eventual production of water (Mokrane et al. 2009; Dulieu et al. 2010; Romanzin et al. 2011):



Finally, a multi-step sequence involving the hydroxylperoxy radical (HO_2) and hydrogen peroxide (H_2O_2) can lead to the formation of water through reactions (5)–(7) (Kaiser et al. 1999; Miyauchi et al. 2008; Ioppolo et al. 2008, 2010; Cuppen et al. 2010):



The recent detection of molecular oxygen (Larsson et al. 2007; Liseau et al. 2012), of the hydroxylperoxy radical (Parise et al. 2012), as well as minute quantities of hydrogen peroxide (Bergman et al. 2011) toward the same source, ρ Oph A, might support the formation of interstellar water through these channels. While reactions (5) and (6) are thought to readily proceed without barrier (Li et al. 2010), reaction (7) is endoergic by around 2300 K (Ellingson et al. 2007).

Here, we investigate an alternative route to the formation of water on interstellar grains and probe to what extent water—in form of perdeuterated water (D_2O)—can be formed via the interaction of mono energetic deuterons (D^+) with solid oxygen ice at 10 K. Note that energetic galactic cosmic ray (GCR) particles can penetrate deep inside cold molecular clouds and transfer their kinetic energy to the surrounding matter (gas, grains). Once decelerated to a few keV, GCRs can be implanted into ices condensed on interstellar grains (Kaiser 2002; Kaiser et al. 1997). This eventually leads to the neutralization of GCRs—here to deuterium atoms—and allows for subsequent reaction of these (suprathermal) particles such as deuterium atoms with molecular oxygen.

2. EXPERIMENTAL

The apparatus utilized for these experiments has been introduced previously (Ennis et al. 2011). The experiments are conducted in ultra-high vacuum chamber evacuated to $9.1 \pm 0.5 \times 10^{-11}$ torr. Neat oxygen ices are condensed onto a silver target (12.4 ± 0.5 K), which has been interfaced to a closed cycle helium refrigerator. The gas-phase is sampled on-line and in situ via a quadrupole mass spectrometer (QMS; Balzer QMG 420) operating in residual gas analyzer mode—ionizing the neutral molecules via electron impact at an energy of 100 eV. The ices are monitored on-line and in situ by a Nicolet 6700 FTIR spectrometer utilizing a liquid nitrogen cooled MCTB detector in absorption–reflection–absorption mode. The molecular oxygen ices were prepared by condensing molecular oxygen (BOC gases; 99.999%) for 20 minutes at 10^{-7} torr

through a glass capillary array. The manufacturer states that the highest impurity in the oxygen gas is argon (Ar) with up to 10 ppm. Since the doubly ionized argon has the same mass-to-charge as singly ionized deuterated water (D_2O^+) ($m/z = 20$), it is crucial to also monitor Ar^+ ($m/z = 40$); this assists to assign $m/z = 20$ either as D_2O^+ and/or Ar^{2+} . Note that the ionization cross-section for Ar^+ is about 14 times larger than for Ar^{2+} at our impact energy (Stephan et al. 1980).

The thickness of the oxygen ice was determined using both the modified Beer–Lambert law applied previously (Bennett et al. 2004) as well as by the Fabry–Pérot relationship as described in Leopold et al. (2009). Considering the diffraction of the incident infrared beam by the modified Beer–Lambert and applying an A -value of 5.0×10^{-21} cm molecule $^{-1}$ (Vandenbussche et al. 1999), an index of refraction of $n = 1.25$ at 20 K (Fulvio et al. 2009), and a density of 1.22 g cm $^{-3}$ (Fulvio et al. 2009), the thickness of the molecular oxygen ice is computed to be 7.0 ± 0.5 μm . The Fabry–Pérot approach takes advantage of the wavelength-dependent interference pattern that becomes apparent in the FTIR spectra when thick ices (several μm) are deposited. The relationship is given as

$$2nd = m_1\lambda_1, \quad (8)$$

where λ_1 represents the wavelength, n is the refractive index and d the ice thickness. The interference order m_1 can be obtained by taking in consideration any two maxima and solving

$$m_1 = \frac{\lambda_2}{\lambda_2 - \lambda_1} \delta m_{12}. \quad (9)$$

Here, the value of δm_{12} takes the value of 1 for consecutive maxima or minima as used here, or 0.5 if adjacent maxima are used. This suggests a thickness of about 3.7 ± 0.2 μm . If an A -value of 9.3×10^{-21} cm molecule $^{-1}$ is adopted for O_2 ice instead, the resulting thickness is determined to be 3.7 ± 0.3 μm ; a value of 1×10^{-20} cm molecule $^{-1}$ is commonly found in the literature (Vandenbussche et al. 1999).

The ices were then irradiated with 5 keV D^+ ions for 72 hr. Singly ionized deuterium is generated in a commercially available ion source (SPECS IQE 12/38) which has been affixed to a differential pumping scheme to minimize residual deuterium gas entering the analysis chamber. Molecular deuterium gas (99.8% D; Icon) was ionized via electron impact at a pressure of 5.0×10^{-4} torr. Since this procedure also produces D_2^+ and D_3^+ ions, the latter have to be separated. All ions at an energy of 5 keV passed through a Wien filter (0.12 T; Specs WF-IQE) so that only 5 keV D^+ ions are selected. The beam current was measured to be 19.3 ± 2.0 nA on the target, which translates to a flux of $1.20 \pm 0.13 \times 10^{11}$ s $^{-1}$; measurements of the beam profile indicate that the area irradiated is 0.5 ± 0.1 cm 2 . Thus, during the irradiation period, the target is exposed to $3.1 \pm 0.3 \times 10^{16}$ ions. The ice target was then left isothermally at 12.4 ± 0.5 K for 30 minutes before being heated to 300 K at a rate of 0.5 K min $^{-1}$.

To calculate the dose, simulations of the energy transfer process and penetration depth were carried out using the TRIM code (Ziegler 1999) using the SRIM-2008 stopping power version. In the simulation, 5 keV D^+ ions (2.014 amu) were directed toward a solid molecular oxygen target with a density of 1.22 g cm $^{-3}$ (Fulvio et al. 2009). The average penetration depth was determined to be 208 ± 39 nm indicating an average dose of 652 ± 139 eV per target molecule. The maximum penetration depth was found to be 500 nm.

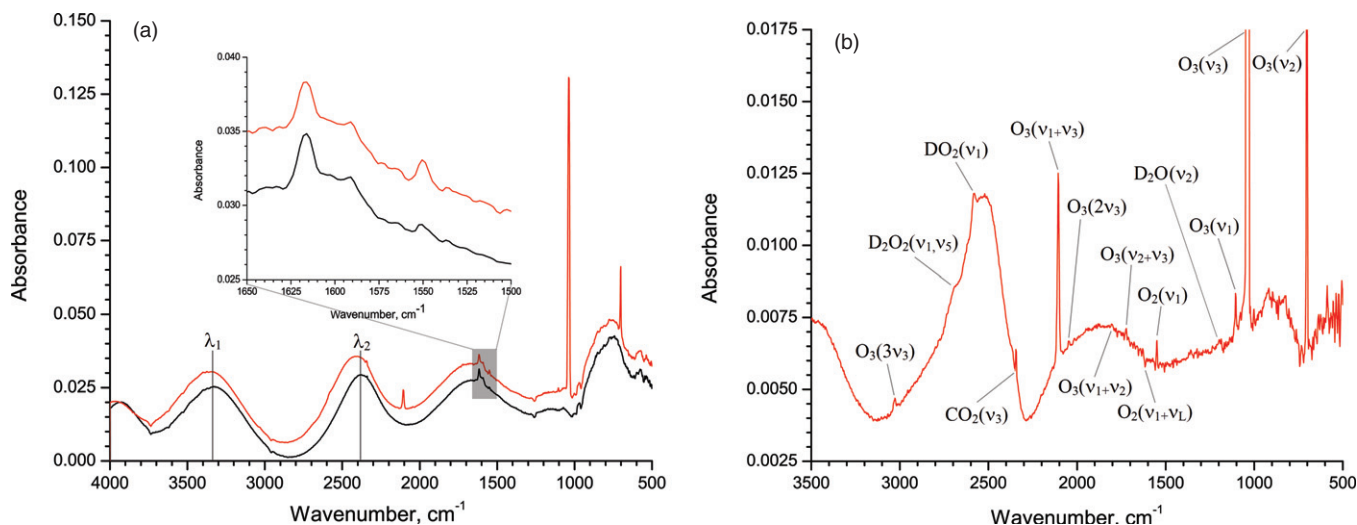


Figure 1. Infrared spectra of oxygen ices: (a) before (black line) and after irradiation (red line) with the positions of the maxima used for the film thickness determination indicated. (b) Difference spectrum before and after irradiation illustrating peak positions of newly formed molecules (Tables 1 and 2).

(A color version of this figure is available in the online journal.)

Table 1

Infrared Absorptions of New Species Formed during the Irradiation Period

Frequency (cm ⁻¹)	Assignment	Characterization
703	O ₃ (ν ₂)	O—O—O bend
1037	O ₃ (ν ₃)	O—O asymmetric stretch
~1043sh	DO ₂ (ν ₂)	D—O—O bend
	D ₂ O ₂ (ν ₂ , ν ₆)	OD symmetric/asymmetric bend
1105	O ₃ (ν ₁)	O—O symmetric stretch
1195 ^a	D ₂ O (ν ₂)	D—O—D bend
1723	O ₃ (ν ₂ +ν ₃)	Combination band
2046 ^b	O ₃ (2ν ₃)	Overtone band
2106	O ₃ (ν ₁ +ν ₃)	Combination band
2472br ^b	D ₂ O (ν ₁ , ν ₃)	Symmetric/asymmetric stretch
2583	DO ₂ (ν ₁)	OD stretch
2707 ^c	D ₂ O ₂ (ν ₁ , ν ₅)	OD symmetric/asymmetric stretch
3029	O ₃ (3ν ₃)	Overtone band

Notes.

^a Shifts toward 1174 cm⁻¹ and broadens during heating after the O₂ matrix has sublimated.

^b Observed only after the O₂ matrix has sublimated.

^c Shifts toward 2676 cm⁻¹ during heating after the O₂ matrix has sublimated.

3. RESULTS AND DISCUSSION

3.1. Identification of New Species during the Irradiation

3.1.1. Ozone (O₃)

Seven absorption bands of ozone were detected (Figure 1; Table 1). The band positions are in excellent agreement with earlier studies (Brewer & Wang 1972; Bennett & Kaiser 2005). In a previous investigation, Bennett & Kaiser (2005) performed irradiation experiments with 5 keV electrons on an oxygen ice held at 10 K, whereby the products were formed through inelastic (S_e) energy transfer processes. This investigation therefore serves as a good comparison for the present set of experiments where nuclear energy transfer processes (S_n) are also expected. The O₃ fundamental bands ν₁, ν₂, and ν₃ are identified at 1105, 703, and 1037 cm⁻¹, compared to those of Bennett & Kaiser (2005) at 1104, 702, and 1037 cm⁻¹, respectively. The overtone bands 2ν₃ and 3ν₃ were detected at 2046, and 3029 cm⁻¹,

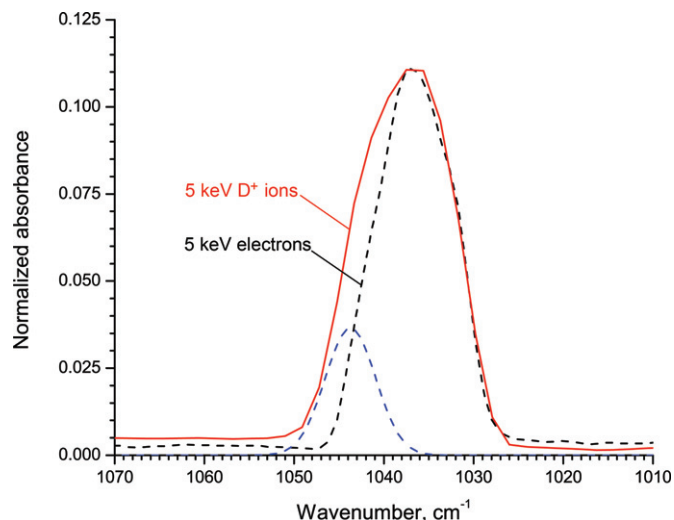


Figure 2. Comparison of the ν₃ band profile of ozone produced after oxygen ices were exposed to energetic deuterons (solid red line; present work) with that produced from irradiation with energetic electrons (dashed black line; taken from Bennett & Kaiser 2005). The spectrum taken from the oxygen ice irradiated with the electrons has been normalized to that of deuteron implanted ice. The smaller Gaussian centered at 1043 cm⁻¹ (blue dashed lines) has been overlaid to demonstrate the approximate position and width of the additional shoulder feature observed with deuterons.

(A color version of this figure is available in the online journal.)

previously identified at 2044 and 3028 cm⁻¹. The combination bands ν₂ + ν₃ and ν₁ + ν₃ were observed at 1723 and 2106 cm⁻¹, formerly observed at 1721 and 2105 cm⁻¹. However, there is one important difference the present and previous experiments (Figure 2). Here, an additional high-frequency band is observed at approximately 1043 cm⁻¹ on the shoulder of the ν₃ fundamental band located at 1037 cm⁻¹. In the previous study, this band was found to be composed not only the O₃ monomer at 1037 cm⁻¹, but also of an O₃...O₃ complex at 1042 cm⁻¹ and an O₃...O complex at 1032 cm⁻¹. Attempts to deconvolute the band into these three components were unsuccessful, indicating that additional species produced in the ice are contributing to this shoulder feature.

3.1.2. Deuterated Hydroperoxyl Radical (DO_2)

Deuterons can undergo neutralization and ultimately thermalize as deuterium atoms. Therefore, we would expect to observe the DO_2 produced through reaction (5). The absorption at 2583 cm^{-1} could be attributed to the ν_1 band of DO_2 ; Cooper et al. (2006) observed shifts in band position of $\sim 40\text{ cm}^{-1}$ between argon and water matrices. The infrared frequencies suggest that the corresponding absorption bands should lie at 2582, 1060, and 1137 cm^{-1} , respectively. Note that the hydroxylperoxyl radical was formed in MeV proton irradiated oxygen–methane ices (Kaiser et al. 1999). Cooper et al. (2006) observed HO_2 when $H_2O:O_2$ (6:1 ratio) ices held at 9 K were exposed to 0.8 MeV H^+ . Cuppen et al. (2010) were also able to observe this species when oxygen ices were exposed to hydrogen atoms. Regarding the deuterated counterpart, Engdahl & Nelander (2004) investigated complexes formed between DO_2 and D_2O_2 that were isolated in Ar matrices held at 17 K. Here, the ν_1 , ν_2 , and ν_3 bands associated with DO_2 were identified at 2530, 1020, and 1123 cm^{-1} . Tso & Lee (1985) showed that within an oxygen matrix at 12–15 K, the same absorptions of DO_2 were identified at 2521–2530, 1019–1024, and $1106\text{--}1123\text{ cm}^{-1}$, respectively.

3.1.3. Deuterium Peroxide (D_2O_2)

The band observed at 2707 cm^{-1} agrees with the band positions of the ν_1 and ν_5 bands of D_2O_2 when isolated within an oxygen matrix; after the sublimation of the oxygen, this band shifts to 2676 cm^{-1} . Previously, D_2O_2 was observed by Miyauchi et al. (2008) in experiments where oxygen ices were exposed to deuterium atoms. They stated that the band at 1033 cm^{-1} was derived from the D_2O_2 molecule along with two additional peaks at 2456 and 2066 cm^{-1} . In a similar experiment, Ioppolo et al. (2008) was able to identify D_2O_2 , unfortunately the band positions were merely stated as being red-shifted $\sim 400\text{ cm}^{-1}$ from the corresponding H_2O_2 values. However, the values roughly agree with those published by Miyauchi et al. (2008). Romanzin et al. (2011) were also able to identify D_2O_2 when ozone ices were exposed to deuterium atoms. Here, they characterized the absorptions corresponding to this species as ν_1 , ν_5 at 2465 cm^{-1} , $2\nu_6$ at 2100 cm^{-1} , $\nu_2/2\nu_4/\nu_6$ at 1050 cm^{-1} , and ν_3 at 884 cm^{-1} . Jing et al. (2011) observed this species at ~ 2400 , 2100, and 1050 cm^{-1} . Lastly, when Oba et al. (2012) condensed what they referred to as “ D_2O fragments” produced during the production of their OD beam, they identified the formation of D_2O_2 through bands observed at 2435, 2115, and $\sim 1050\text{ cm}^{-1}$. Note that the band positions reported above display higher correlation to those originating from pure D_2O_2 ices rather than D_2O_2 isolated within an inert matrix. The band-widths are also much broader than expected for matrix isolated species, as D_2O_2 is produced at the surface in these experiments.

3.1.4. Deuterated Water (D_2O)

The strongest absorption for D_2O isolated within an oxygen matrix is the ν_2 band occurring at about 1200 cm^{-1} . Matrix isolation studies showed this feature absorbs at 1177 cm^{-1} within a carbon monoxide matrix (Tso & Lee 1985), and at 1179 and 1182 cm^{-1} isolated within an argon matrix (Ceponkus & Nelander 2004; Dozova et al. 2006). In the present experiments, the 1195 cm^{-1} absorption band is found to grow during the latter part of the irradiation. This peak position is in good agreement with the above studies and confirms the presence of D_2O . The

formation of D_2O has previously been demonstrated in experiments where oxygen ices were exposed to deuterium atoms (Ioppolo et al. 2008; Miyauchi et al. 2008; Oba et al. 2009). D_2O also forms when deuterium atoms are co-condensed with oxygen atoms (Jing et al. 2011). The characteristic absorptions identified at $\sim 2400\text{ cm}^{-1}$ (ν_1 , ν_3) and $\sim 1200\text{ cm}^{-1}$ (ν_2) correlate with those observed for pure D_2O ices (Bertie & Whalley 1964; Bergren et al. 1978; Zheng et al. 2007). Our experimental conditions favor the production of D_2O within a matrix of oxygen rather than forming the pure D_2O ice.

3.2. Observations during the Warm-up of the Irradiated Ice

3.2.1. O_2 and O_3

The oxygen ice sublimates at 25 K, where the FTIR band area begins to decrease from its initial column density of $1.09 \times 10^{19}\text{ molecules cm}^{-2}$ to be undetectable beyond 42 K (Figure 3(a); thick gray line). Gas-phase molecular oxygen is observed via the molecular ion peak (O_2^+ ; $m/z = 32$; thick gray line) that begins to rise steeply at 25 K before climaxing at approximately 37 K and thereafter slowly decaying as this species is pumped out of the chamber. These values agree well with a previous study in our group (Bennett & Kaiser 2005), where the oxygen ice was found to sublimate over the range of 28–43 K. Note that at the same time, a peak corresponding to the ozone molecular ion (O_3^+ ; $m/z = 48$; blue filled squares) is simultaneously observed (Figure 4(a)). Whilst some of this signal may be due to ozone sublimating with the bulk of the ice, the majority of ozone detected here is produced via ion–molecule reactions occur within the ionizer of the mass spectrometer (see Bennett & Kaiser 2005 for further details). In addition, both peaks reappear between 47 and 67 K peaking at 62 K (Figure 4(a)). In this case, the molecular oxygen peak is a result of fragmentation of ozone caused by electron-impact dissociation. This is consistent with the FTIR observations of the ozone peak (Figure 3(a); red dashed line), which is shown to decrease over approximately the same temperature range but not during the desorption of molecular oxygen.

3.2.2. D_2O_2

At 25 K, when the oxygen ice sublimates, the ν_1 , ν_5 D_2O_2 band area increases by about 75%. However, at approximately 50 K, the band area abruptly decreases before being no longer observable in the solid state at 70 K (Figure 3(a); black line); suggesting that deuterium atoms might react with DO_2 to form D_2O_2 . Alternatively, the A -value for D_2O_2 could rise as the O_2 ice sublimates. As noted in the Appendix, the change in the A -values between matrix isolated and the pure D_2O_2 ice provides some evidence for this argument. It is expected that this deuterated hydrogen peroxide should be detectable in the gas-phase. However, Figure 4(b) shows the signal for $D_2O_2^+$ ($m/z = 36$) and displays only a slight increase in signal over the corresponding temperature range. The majority of the signal for this species is in fact observed over 25–42 K. Note that pure D_2O_2 ice has been shown to sublime at approximately 180 K (Loeffler et al. 2006).

3.2.3. D_2O

As discussed in Section 2, argon is a known contaminant of the oxygen gas used. Since the D_2O molecular ion (D_2O^+ ; $m/z = 20$) is at the same mass as doubly ionized argon (Ar^{2+} ; $m/z = 20$), it is essential to simultaneously monitor the singly ionized argon species (Ar^+ ; $m/z = 40$). During the sublimation of the oxygen ice between 25 and 45 K, there

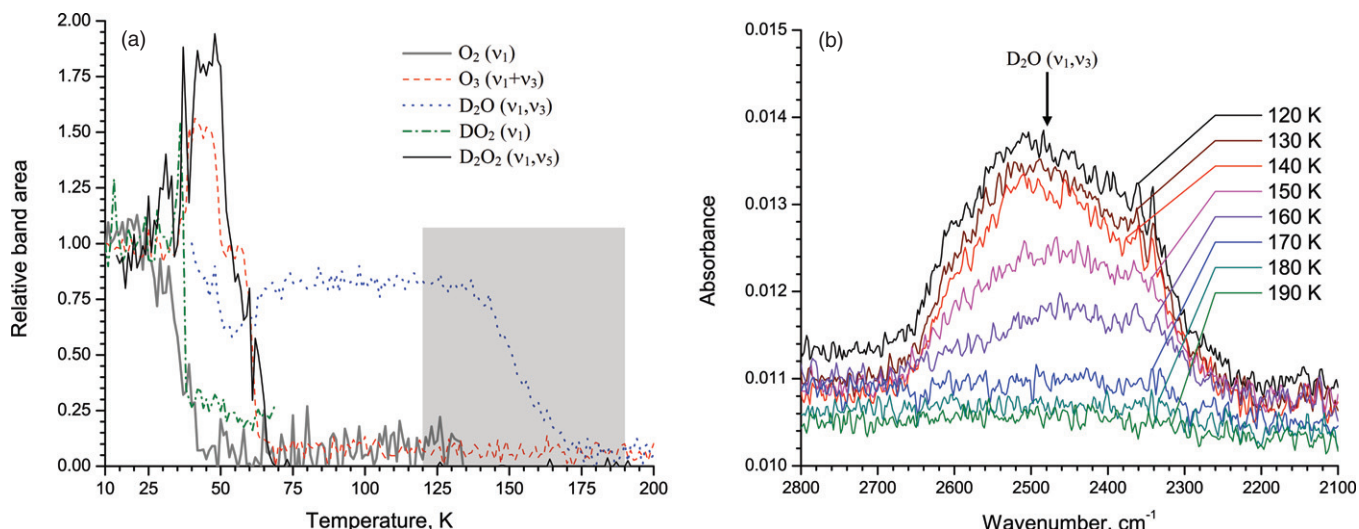


Figure 3. (a) Temporal evolution of the band areas during the warm up period for O₂ (thick gray line), O₃ (dashed red line), DO₂ (dot-dashed green line) D₂O₂ (black line), and D₂O (dotted blue line; traced only after 40 K). (b) The FTIR spectra in the 2100–2800 cm⁻¹ are shown between the temperature range of 120–190 K at 10 K intervals to demonstrate the decrease of the D₂O (ν₁, ν₃) band as this molecule sublimates; this region is highlighted in gray on panel (a).

(A color version of this figure is available in the online journal.)

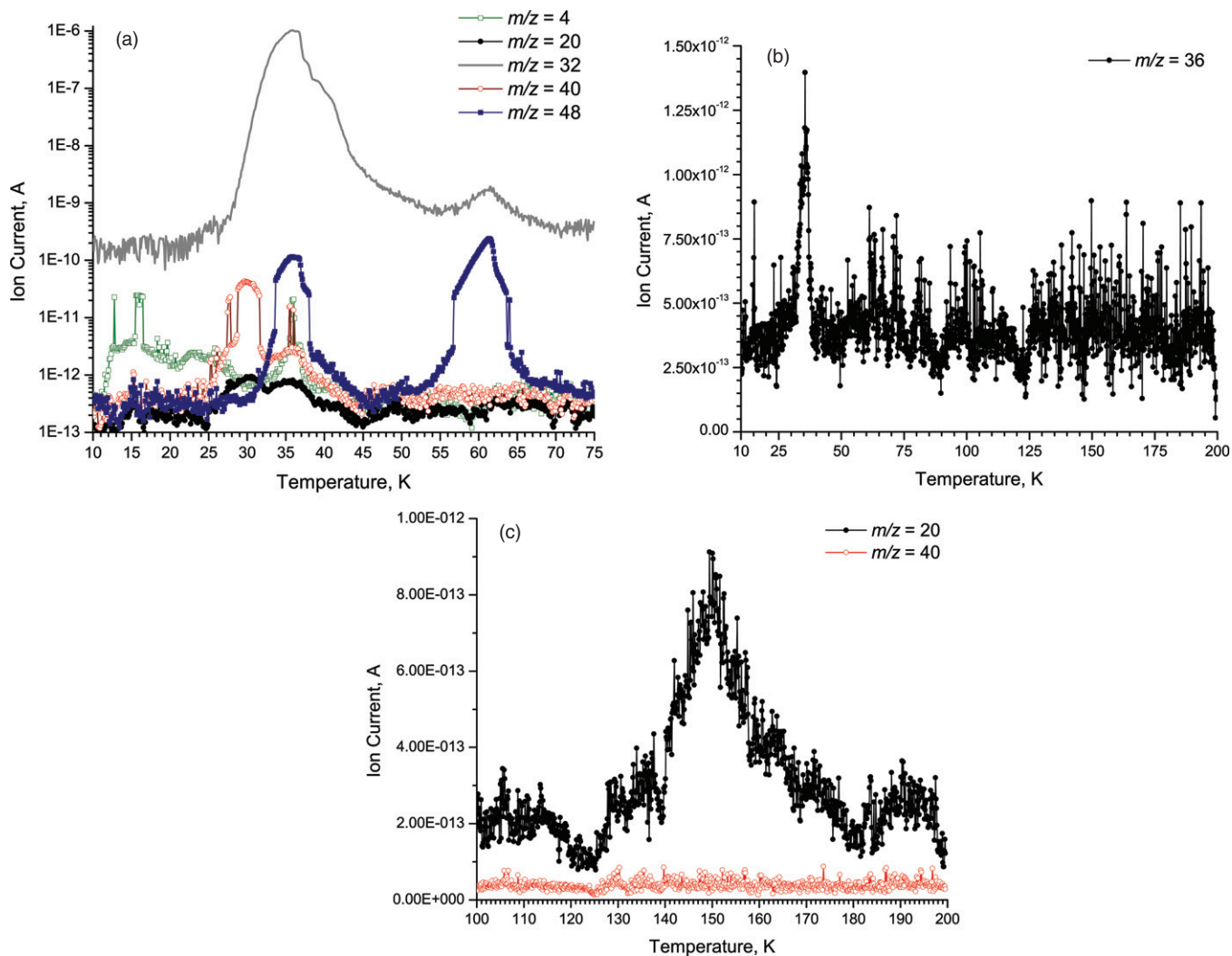


Figure 4. Ions monitored by the QMS during the sublimation of the irradiated ice: (a) from 10–75 K showing the profiles of D₂⁺ (m/z = 4; green line, open squares), D₂O⁺/Ar²⁺ (m/z = 20; black line, closed circles), O₂⁺ (m/z = 32; thick gray line), Ar⁺ (m/z = 40; red line, open circles), and O₃⁺ (m/z = 48; blue line, closed squares); (b) from 10–200 K for D₂O₂⁺ (m/z = 36; black line, closed circles)—separated for clarity; and (c) from 100–200 K for D₂O⁺ (m/z = 20; black line, closed circles) and Ar⁺ (m/z = 40; red line, open circles).

(A color version of this figure is available in the online journal.)

Table 2
Infrared Intensities (A Values) Used in This Study

Species	Band Position	Carrier	A Value (cm molecule^{-1})
O_3	2112	$\text{O}_3 (\nu_1 + \nu_3)$	1.5×10^{-18}
D_2O_2	2621, 2623	$\text{D}_2\text{O}_2 (\nu_1, \nu_5)$	5.8×10^{-18}
DO_2	2585	$\text{DO}_2 (\nu_1)$	7.4×10^{-18}
D_2O	2633, 2747	$\text{D}_2\text{O} (\nu_1, \nu_3)$	6.2×10^{-18a}
OD	2612	$\text{OD} (\nu_1)$	1.5×10^{-18}

Notes. See the [Appendix](#) for additional details.

^a A value was used during irradiation, but for quantification after the O_2 matrix has sublimed, an A value of 1.4×10^{-16} was used for the pure D_2O ice (Berggren et al. 1978).

appears to be two small peaks for both the $m/z = 20$ and $m/z = 40$ channels arising at a substrate temperature between approximately 30 and 35 K (Figure 4(a)). Since there is a peak at $m/z = 40$ in both cases we can conclude that at least some of this is due to argon. Figure 4(c) shows both the ion currents recorded for the mass spec at $m/z = 20$ and $m/z = 40$ over the temperature range of 100–200 K. Here, it can clearly be seen that an increase in signal $m/z = 20$ is observed over the range 120–180 K, peaking at 150 K, whilst the signal at $m/z = 40$ remains flat indicating that this is purely due to D_2O . This is in perfect agreement with the previously reported values for the sublimation temperatures of pure D_2O ices (Zheng et al. 2007). The temporal FTIR profile garners additional support for the detection of D_2O . Above 40 K, the ν_1 , ν_3 band of D_2O also becomes observable at 2472 cm^{-1} , along with the previously identified ν_2 band which shifts to 1174 cm^{-1} after the oxygen ice has sublimated. These features suggest pure D_2O ice. In fact, no other species were detectable within the ice beyond the O_3 sublimation temperature at 68 K. The temporal profile for D_2O is shown in Figure 3(a) (blue dotted line). The region from 120–180 K (highlighted in gray) shows the D_2O band diminishing at the same time that D_2O is sampled in the gas-phase. To clarify this, FTIR spectra of the ν_1 , ν_3 band of D_2O at 2472 cm^{-1} is shown at 10 K intervals over this temperature range, displaying the decrease in the solid state (Figure 3(b)). The ν_2 band indicates that at the end of irradiation, there were approximately $1.0 \times 10^{15} \text{ molecules cm}^{-2}$ of D_2O , whereas once the ν_1 , ν_3 band becomes observable, the column density using the pure solid state value (Table 2) indicates approximately four times this value. This discrepancy can be explained by either the production of additional D_2O molecules, or by a disparity between A values utilized for the two bands (see the [Appendix](#) for additional details).

3.2.4. D_2

A signal is observed from the onset of heating due to D_2^+ ($m/z = 4$; Figure 4(a), green open squares) prior to the sublimation of the O_2 ice. This indicates that an amount of highly volatile D_2 molecules have been formed and subsequently trapped within the ice. The increase in signal at $m/z = 4$ is observed as early as 11 K, and peaks at approximately 16 K, although a large fraction is also released with the majority of the oxygen ice at approximately 37 K.

3.3. Chemical Modeling of Reactions Induced by Irradiation

Having assigned the infrared carriers of the newly formed molecules and quantified the column densities of the newly formed molecules (Figure 5), we are attempting now to elucidate the underlying reaction mechanisms of how these species

are synthesized in the ices during the irradiation. For this purpose, nine kinetic reaction schemes (Models A–I) were developed to fit the column densities of species produced during the irradiation. Systems of up to 11 coupled differential equations from those listed in Table 3, where each of R1–R22 represents the reactions within the ices. This was numerically solved by an iterative procedure for each system (Frenklach 1984; Frenklach et al. 1992, 2007). This approach results in up to 11 rate constants per system as compiled in Table 3; the approach taken in most instances was to fit using a minimum number of required pathways to demonstrate the feasibility of each different approach taken. Reactions between pure oxygen species, R1 to R5, are important in electron and proton irradiated oxygen ices as demonstrated previously in our group (Bennett & Kaiser 2005). Here, reaction R1 presents a decomposition of molecular oxygen into two oxygen atoms with R5 being the back reaction. The bond cleavage is initiated by the impinging irradiation and can bear suprathreshold atomic oxygen species with up to 1–2 eV (1 eV = 11,604.5 K) which can allow them to participate in reactions that possess reaction barriers but may not be feasible in the ISM unless generated through radiolysis. Ozone is formed and destroyed via reactions R2 and R3 as well as R4, respectively. Model B demonstrates that utilizing reactions R4 and R5 gives essentially equivalent results to those from Model A where only R3 accounts for the destruction of ozone. Therefore the remaining models utilize exclusively R3, since it is not possible to differentiate which is actually occurring here. Model C differs from Model A only by the omission of R17 demonstrating that this reaction is not essential here to reproduce the D_2O column density as seen in Figure 5(d). Model D introduces a destruction pathway for D_2O , R19; the radiolysis-induced dissociation into D_2 and $\text{O}(^1\text{D})$. Note that the alternative dissociation pathway into OD and D is more likely and gives almost an identical fit. However, R19 is shown here since this additionally demonstrates a viable route to the formation of D_2 as observed in the mass spectrometer during the warm-up of the ice. Model E varies from Model A in two ways. Firstly, the formation of the DO_2 radical through the recombination of the OD radical and an O atom, R8, is removed. This reaction is predicted to be barrier-less by the calculations of Li et al. (2010), and although is likely occurring to some extent within our ice the exclusion of it here demonstrates that it is not essential; however it was kept in the majority of models since it did improve the overall fits for each species. Secondly, Model E also includes a reaction initiated by a slowed deuterium atom (<10 eV) which is now of low enough energy to participate in suprathreshold chemical reactions (Kaiser 2002). Here, the slowed D atom subtracts an O atom from ozone to regenerate molecular oxygen and an excited OD radical, since the reaction is highly exoergic

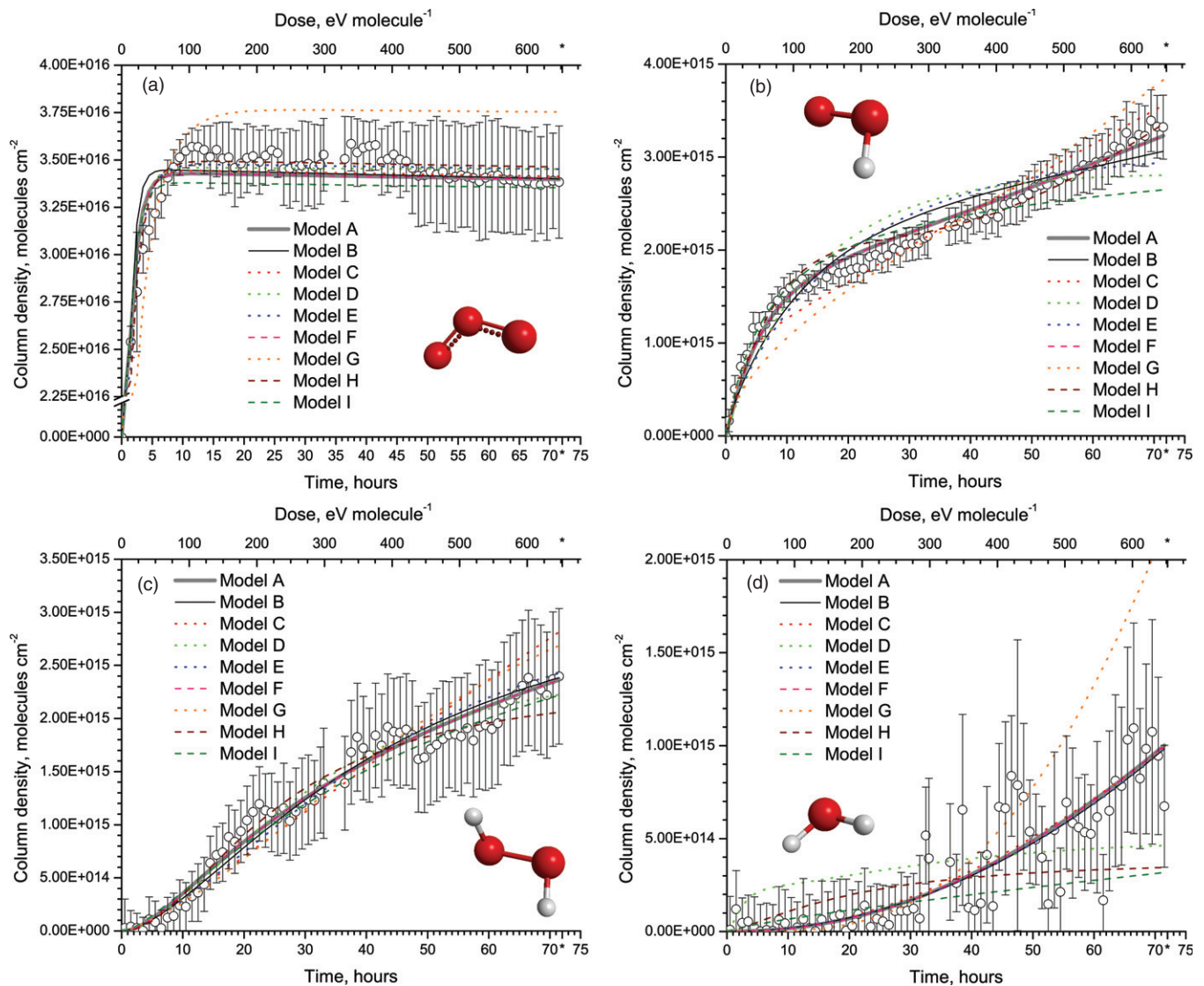


Figure 5. Temporal profiles of the column densities during the irradiation period for (a) O₃, (b) DO₂, (c) D₂O₂, and (d) D₂O. The kinetic fits are also shown for each species according to the reaction schemes listed in Table 4.

(A color version of this figure is available in the online journal.)

(Fernández-Ramos & Varandas 2002). The formation of D₂O through the reaction of D atoms with previously formed D₂O₂ molecules (R15), as discussed in the introduction, is examined in Model F. Here, reaction R15 is the only production pathway to form D₂O in this model in order to demonstrate whether or not it is able to solely account for D₂O production. Recall however, that R15 has a barrier of ~ 2300 K (Ellingson et al. 2007). Since energetic D atoms were utilized in this experiment, the barrier can of course be overcome. But is this reaction viable in the ISM? Although some authors have debated the importance of tunneling reactions which may enhance the ability for H to overcome such a barrier we instead chose here to investigate alternative reactions that could form D₂O without requiring non-thermal pathways. An example is given in Model G, where it is found that when the OD radical reacts with D₂O₂, the barrier to produce D₂O and DO₂ is only found to be 50–100 K (R16; Ginovska et al. 2007). Since R9 is able to produce vibrationally excited OD radicals, by reaction of D atoms with ozone, this pathway was also included. In fact, to demonstrate

that this could be the sole source of OD radicals, the radiolysis-induced destruction of D₂O₂ into two OD radicals (R14) was also excluded from this model. Note that this dissociation pathway (R14) of D₂O₂ is thought to be favored over the generation of DO₂ + D as it lies lower on the potential energy surface (Ge et al. 2006). The fact that Model G is able to overproduce the production of D₂O without any destruction pathways for either D₂O or D₂O₂ included (that would increase the goodness-of-fit) indicates that this reaction could be readily occurring within our ices, and is also applicable to the ISM. Model H shows that D₂O could potentially be the precursor to D₂O₂ by incorporating the barrier-less insertion of a suprathermal O(¹D) atom (R13; Ge et al. 2006), which could be generated through R1 (see Bennett & Kaiser 2005). The alternative pathway via the addition of D atoms to DO₂ (R12) was removed in Model H to investigate if R13 could serve as the only pathway toward D₂O₂ formation. However, the resulting fits were always found to be poorer than those where D₂O₂ formed prior to D₂O invoking this pathway.

Table 3
Summary of Reaction Rates Derived for Each Considered Reaction Scheme Labeled as Models A-I

#	Reaction	Barrier, K	Rate ^a								
			Model A	Model B	Model C	Model D	Model E	Model F	Model G	Model H	Model I
R1	O₂ → O + O	60,000^{c,d}	4.46×10^{-6}	2.84×10^{-6}	4.13×10^{-6}	4.19×10^{-6}	3.64×10^{-6}	4.40×10^{-6}	1.90×10^{-6}	3.41×10^{-6}	4.79×10^{-6}
R2	O ₂ + O → O ₃	~0 ^e	1.18×10^{-20}								
R3	O ₃ + O → 2O ₂	2320 ^f	4.83×10^{-19}	...	4.81×10^{-19}	4.79×10^{-19}	4.69×10^{-19}	4.80×10^{-19}	4.25×10^{-19}	4.74×10^{-19}	4.91×10^{-19}
R4	O₃ → O₂ + O	12,200^{c,d}	...	8.94×10^{-4}
R5	O + O → O ₂	0 ^d	...	1.15×10^{-18}
R6	O ₂ + D → DO ₂	0 ^g	1.09×10^{-19}	2.59×10^{-19}	3.31×10^{-19}	6.98×10^{-21}	4.69×10^{-19}	2.39×10^{-18}	3.04×10^{-20}	8.90×10^{-20}	4.35×10^{-21}
R7	O ₂ + D → OD + O	8150 ^g	4.99×10^{-20}	...
R8	OD + O → DO ₂	~0 ^g	9.38×10^{-21}	4.46×10^{-22}	4.07×10^{-20}	1.56×10^{-23}	...	2.36×10^{-20}	...	1.23×10^{-20}	...
R9	D + O ₃ → OD + O ₂	80 ^h	1.72×10^{-16}	...	3.65×10^{-17}
R10	DO₂ → OD + O	32,300^{c,g}	2.90×10^{-5}	7.80×10^{-6}	9.21×10^{-5}	3.17×10^{-6}	2.06×10^{-6}	2.41×10^{-5}	...
R11	DO ₂ + O → OD + O ₂	~0 ⁱ	1.70×10^{-19}
R12	DO ₂ + D → D ₂ O ₂	0 ^j	2.53×10^{-17}	8.29×10^{-17}	4.39×10^{-17}	2.37×10^{-18}	1.72×10^{-16}	5.17×10^{-16}	1.56×10^{-16}	...	9.65×10^{-19}
R13	D ₂ O + O → D ₂ O ₂	0 ^j	1.01×10^{-18}	...
R14	D₂O₂ → OD + OD	8120^{c,j}	1.08×10^{-5}	9.78×10^{-6}	6.38×10^{-6}	7.61×10^{-6}	8.59×10^{-6}	1.48×10^{-5}	...	4.76×10^{-5}	...
R15	D + D ₂ O ₂ → D ₂ O + OD	2320 ^k	1.09×10^{-16}
R16	OD + D ₂ O ₂ → DO ₂ + OD	50–100 ^l	4.89×10^{-22}
R17	O + D → OD	0 ^o	1.65×10^{-16}	2.23×10^{-16}	...	1.42×10^{-17}	3.10×10^{-17}	8.01×10^{-18}	6.65×10^{-19}
R18	OD + D → D ₂ O	0 ^o	9.64×10^{-19}	3.31×10^{-18}	1.98×10^{-18}	4.15×10^{-17}	7.32×10^{-19}	4.36×10^{-17}	...
R19	D₂O → D₂ + O	81,300^{c,m}	1.22×10^{-4}
R20	OD + OD → D ₂ O + O	0 ⁿ 800 ^j	9.95×10^{-16}
R21	DO ₂ + D → D ₂ + O ₂	750 ⁿ	1.97×10^{-18}
R22	D ₂ O ₂ + D → DO ₂ + D ₂	4600 ^k	8.67×10^{-19}
	Error [O ₃] ^b		0.0441	0.0603	0.0347	0.0330	0.0272	0.0367	0.5015	0.0285	0.0804
	Error [DO ₂] ^b		0.0698	0.2475	0.1661	0.5199	0.3500	0.0612	0.5169	0.0830	0.4884
	Error [D ₂ O ₂] ^b		0.2056	0.2556	0.7761	0.2060	0.3275	0.6443	0.7009	0.2463	0.2524
	Error [D ₂ O] ^b		1.6629	1.6463	1.6637	4.197	1.6428	1.6646	13.1117	4.6775	5.4475

Notes. (Results are shown in Figure 6; details are given in Section 3.4). The barrier for reactions R1-R22 is also given in Kelvin. Reactions stated in bold are dissociation events initiated by the radiolysis process. The rate constant for R2 (O₂ + O → O₃; italicized) was fixed for each model during the iterative fitting procedure, for ease of comparison. The individual errors for each species are given for each model.

^a Unimolecular reactions (A → B) are in units of s⁻¹; bimolecular reactions (A + B → C) are in units of cm² molecules⁻¹ s⁻¹; note that the typical units for the rate of a bimolecular reaction of cm³ molecules⁻¹ s⁻¹ are not applicable here, as our “concentrations” are presented in terms of column densities (molecules cm⁻²) rather than concentration (molecules cm⁻³).

^b Normalized residual sum-of-squares.

^c Reaction proceeds through radiation-induced bond cleavage.

^d Bennett & Kaiser (2005).

^e Ayouz & Babikov (2013); Dawes et al. (2011).

^f Moravej et al. (2006).

^g Li et al. (2010).

^h Fernández-Ramos & Varandas (2002).

ⁱ Silveira et al. (2004).

^j Ge et al. (2006), for R13 this is specific to the singlet potential energy surface.

^k Ellingson et al. (2007).

^l Gínovska et al. (2007).

^m Okabe (1978).

ⁿ Oba et al. (2012).

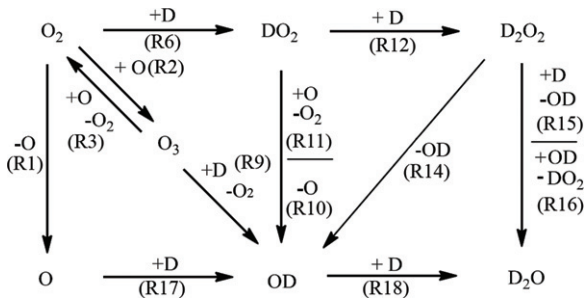


Figure 6. Compilation of reaction pathways leading ultimately to D₂ water in deuterium-irradiated oxygen ices.

Additionally, it was found that the formation of D₂O₂ by the recombination of OD radicals could not reproduce the D₂O₂ column density (not shown here; however, the profile resembled that of D₂O in Model I, discussed next). Instead, the recombination of OD radicals can alternatively produce D₂O (and an O atom) as shown in R20. The resulting profile was included in Model I, and could approximately explain the production of D₂O (Figure 5(d)), but again the errors were found to be large for D₂O indicating that this pathway is perhaps less likely than some of the others suggested. Model I additionally included two additional pathways that could lead to the formation of D₂; reactions R21 and R22. These (along with R19 in Model D) demonstrate that D₂ production could be occurring during the implantation of D atoms into an oxygen ice, which may then additionally be released during the subsequent warm-up as observed here (Figure 4(a)).

4. ASTROPHYSICAL IMPLICATIONS

We have demonstrated that the deuterated analogs of HO₂, H₂O₂, and H₂O can be produced by the implantation of 5 keV D⁺ ions into molecular oxygen ices at 12.4 ± 0.5 K. Recall that energetic GCRs penetrate deep inside molecular clouds to interact with ices as condensed on interstellar grains. If embedded within outer apolar layers of icy grains, where molecular oxygen is expected to be the major constituent (Ehrenfreund et al. 1997), charged particles can transfer their kinetic energy initially via inelastic interaction and, once slowed down to a few keV, also via nuclear interactions. Slowed down even further, charged particles can be neutralized, in the present case, to suprathreshold deuterium atoms holding kinetic energies of a few eV. Therefore, GCRs and the deuterium atoms can interact with molecular oxygen and trigger reaction pathways as compiled in Figure 6. Common patterns leading to D₂ water formation can be extracted. Considering Models A to C, D₂ water is eventually formed via the recombination of OD radicals with atomic deuterium (R18). Here the OD radicals can be synthesized via three pathways: (1) recombination of atomic oxygen and deuterium, O + D (Model A), (2) the reaction sequence O₂ + D → DO₂ → D₂O₂ → 2 OD (Models A/C), and (3) O₂ + D → DO₂ → OD (Models A/C). In Model F, OD can be also accessed via oxygen abstraction through the reaction of DO₂ with atomic oxygen. In Models E and G, the formation of OD was demonstrated through the reaction of atomic deuterium with ozone, O₃. This reaction (R9) exhibits a barrier of only ~80 K and could therefore be accessible in the ISM, and additionally is shown to form vibrationally excited OD radicals. Model G also demonstrated that this opens up another accessible pathway to the formation of D₂O through the reaction of OD with D₂O₂ (R16). The reaction barrier here is

only estimated to be 50–100 K. The formation of D₂O₂ itself likely occurs through the sequential addition of deuterium atoms to molecular oxygen, O₂, forming DO₂ and then D₂O₂ through the barrier-less reactions R6 and R12, respectively. It is worth noting that the formation of O₃ is expected to occur within icy grains since the addition of O to O₂ is barrier-less and also O₃ is formed when O₂ ices are exposed to GCR radiation (Bennett & Kaiser 2005). Therefore, that D₂O can form through the reactions in Model G suggests that if ozone is present, the formation of water is possible even if only thermal hydrogen atoms are available to react, impinging on the surface of the grain from the ISM. Model F also shows that the alternative pathway to D₂ water via suprathreshold deuterium atom reactions with D₂O₂ (R15) previously suggested is a viable alternative if indeed tunneling is efficient enough to overcome the barrier of ~2300 K. Therefore, our laboratory studies provide important constraints in the underlying reaction pathways leading to the formation of water ices on interstellar grains.

This material was based upon work supported by the National Aeronautics and Space Administration (NASA Astrobiology Institute under Cooperative Agreement No. NNA09DA77A issued through the Office of Space Science).

APPENDIX

A.1. Derivation of Infrared Intensities (A Values)

Much of the analysis presented in this work—as well the interpretation of spectral features for column density calculations pertinent to astrophysical phenomena—is dependent upon the quantification of products based on the inferred strength of infrared absorption features. It is therefore essential that these values be as accurate as possible. Solid-state measurements have been made for pure H₂O (Hudgins et al. 1993; Gerakines et al. 1995), pure H₂O₂ (Smith et al. 2011), and pure O₃ (Raut et al. 2011). In general, an enhancement (up to ~30 times for both H₂O and H₂O₂) of the solid-state intensity is observed, compared to the associated gas-phase value. Ab initio calculations on small (H₂O)₁₀ clusters do show evidence for an increased infrared intensity compared to values determined for a single H₂O molecule (e.g., Wang & Bowman 2011). The precise reason for these enhancements requires further investigation, but is likely influenced by both the dielectric susceptibility, ϵ , of the medium and intramolecular interactions such as lattice formation, hydrogen bonding, Van der Waals complexes, etc. Pilla et al. (2008) recently measured the dielectric susceptibility, ϵ , of molecular oxygen frosts down to 4 K, and found the value to be approximately 1.5; much closer to the value of an isolated molecule in vacuo, $\epsilon = 1.0$) than that measured for pure solids of H₂O, H₂O₂ and O₃ (e.g., H₂O, $\epsilon > 80.0$; Aragonés et al. 2011). Therefore, the measurements previously made for the pure ices cannot be directly used. Corresponding measurements for the infrared intensities of their deuterated counterparts have not been made (as discussed by Miyauchi et al. 2008). Where the measurement of the infrared intensity of radicals is concerned, since they are not stable and are produced in situ (often with assumptions made about their formation or destruction rates), these are far less accurate.

Note, however, that infrared intensities calculated by high-level ab initio or density functional theory (DFT) for small molecules are found to be accurate to within 20% of the reported

Table 4
Compiled Experimental and Calculated Values for the Vibrational Frequencies and Intensities of Water (H₂O) and Its Deuterated Counterpart (D₂O)

Mode	Experimental Values				Calculated Values						Best Estimated Values	
	H ₂ O(g) ^a		H ₂ O(s) ^b		H ₂ O ^c		H ₂ O, PCM ($\Sigma = 1.5$) ^c		D ₂ O ^c		D ₂ O(O ₂)	
	Freq, cm ⁻¹	A Value, cm molecule ⁻¹	Freq, cm ⁻¹	A Value, cm molecule ⁻¹	Freq, cm ⁻¹	A Value, cm molecule ⁻¹	Freq, cm ⁻¹	A Value, cm molecule ⁻¹	Freq, cm ⁻¹	A Value, cm molecule ⁻¹	Freq, cm ⁻¹	A Value, cm molecule ⁻¹
ν_1	3657	4.8×10^{-19}	3280 ^d	2.0×10^{-16d}	3806	6.6×10^{-19}	3802	1.2×10^{-18}	2743	5.5×10^{-19}	2633 ^e	7.0×10^{-19f}
ν_2	1595	1.0×10^{-17}	1660	1.2×10^{-17}	1634	1.2×10^{-17}	1629	1.4×10^{-17}	1197	6.4×10^{-18}	1165 ^e	6.3×10^{-18}
ν_3	3756	6.9×10^{-18}	3280 ^d	2.0×10^{-16d}	3906	8.6×10^{-18}	3898	1.1×10^{-17}	2863	5.4×10^{-18}	2747 ^e	5.5×10^{-18f}

Notes. Best estimate frequency and intensity values are also listed; calculated via the scheme described in the text. Italicized values were not used in the best estimate calculations and are given for comparison only.

^a Taken from the NIST CCCBDB database, <http://cccbdb.nist.gov/> (release 15b, updated 2011 August).

^b Taken from Gerakines et al. (1995).

^c B3LYP/cc-pVQZ (harmonic).

^d Overlapping bands. Intensities given are the sum of both bands.

^e Based on gas-phase positions. Frequencies determined from solid state band positions for are ν_1 , ν_2 , and ν_3 are 2364, 2404, and 1216 cm⁻¹, respectively.

^f Combined intensity is 6.2×10^{-18} cm molecule⁻¹.

Table 5

Compiled Experimental and Calculated Values for the Vibrational Frequencies and Intensities of Hydrogen Peroxide (H₂O₂) and Its Deuterated Counterpart (D₂O₂)

Mode	Experimental Values				Calculated Values						Best Estimated Value	
	H ₂ O ₂ (g)		H ₂ O ₂ (s) ^a		H ₂ O ₂ ^b		D ₂ O ₂ ^b		D ₂ O ₂ , PCM ($\Sigma = 1.5$) ^b		D ₂ O ₂ (O ₂)	
	Freq, cm ^{-1c}	A Value, cm molecule ^{-1d}	Freq, cm ⁻¹	A Value, cm molecule ⁻¹	Freq, cm ⁻¹	A Value, cm molecule ⁻¹	Freq, cm ⁻¹	A Value, cm molecule ⁻¹	Freq, cm ⁻¹	A Value, cm molecule ⁻¹	Freq, cm ⁻¹	A Value, cm molecule ⁻¹
ν_1	3599	8.5×10^{-18e}	3241 ^e	2.0×10^{-16e}	3766	2.1×10^{-18}	2746	1.1×10^{-18}	2743	1.6×10^{-18}	2621	5.8×10^{-18e}
ν_2	1402	1439	...	1054	...	1047	...	1020	...
ν_3	877	1.7×10^{-19}	885	6.0×10^{-19}	951	1.3×10^{-19}	948	5.0×10^{-20}	949	5.0×10^{-20}	875	6.6×10^{-20}
ν_4	371	380	...	278	...	278	...	271	...
ν_5	3608	8.5×10^{-18e}	3241 ^e	2.0×10^{-16e}	3765	8.8×10^{-18}	2741	4.7×10^{-18}	2737	5.9×10^{-18}	2623	5.8×10^{-18e}
ν_6	1266	1.8×10^{-17}	1364	1.8×10^{-17}	1327	1.7×10^{-17}	982	8.4×10^{-18}	988	9.3×10^{-18}	943	9.8×10^{-18}

Notes. Best estimate frequency and intensity values are also listed; calculated via the scheme described in the text. Italicized values were not used in the best estimate calculations and are given for comparison only.

^a Taken from Smith et al. (2011).

^b B3LYP/cc-pVQZ (harmonic).

^c Taken from the NIST CCCBDB database, <http://cccbdb.nist.gov/> (release 15b, updated 2011 August).

^d Taken from Johnson et al. (2009).

^e Overlapping bands. Intensities given are the sum of both bands.

gas-phase values (Galabov et al. 2002). Recent developments that more accurately treat anharmonicity on the potential energy surface with a sufficiently high level of theory can reduce the error further (e.g., Seidler et al. 2007). Here, the GAMESS(US) software package (Schmidt et al. 1993; Gordon & Schmidt 2005) was used to calculate a series of “correction factors” to determine the ratios by which the infrared intensities and vibrational frequencies of molecular species are altered when (1) they are deuterated, and (2) solvated within a matrix that simulates the surrounding O₂ ice. In the case of radical species, high-level calculations were chosen as starting values in preference to experimental values, due to their inherent high level of uncertainty. Equation (A1) shows how this general approach can be applied to calculate the infrared intensity for D₂O within an O₂ matrix, $I[D_2O_{(O_2)}]$:

$$I[D_2O_{(O_2)}] \approx I[H_2O_{(g)}] \times \frac{I[D_2O]}{I[H_2O]} \times \frac{I[H_2O_{(PCM, \epsilon=1.5)}]}{I[H_2O]} \quad (A1)$$

Where the original infrared intensities are here taken from experimentally determined values for H₂O in the gas phase, $I[H_2O_{(g)}]$. To apply a correction for the deuterated species,

both the H₂O molecule and D₂O molecule intensities are calculated and the original values are multiplied by this ratio, $I[D_2O]/I[H_2O]$. Similarly, the correction for the species being isolated within a matrix of O₂ is then calculated by determining the effect of the surrounding O₂ matrix on the infrared intensities, $I[H_2O_{(PCM, \epsilon=1.5)}]$, by using the polarizable continuum model (PCM; see Tomasi et al. 2005) where ϵ is set to a value of 1.5. To determine these correction factors, high accuracy is not important, since the same errors will be consistently produced for both calculated values. This allows a cheaper computational method, such as DFT, to be used with little need to go beyond the harmonic approximation. The PCM is also compatible with DFT calculations. Due to its high accuracy in predicting infrared frequencies and intensities, the hybrid B3LYP level of theory was chosen (Lee et al. 1988; Becke 1993; Stephens et al. 1994); employing the correlation consistent quadruple-zeta dunning (cc-pVQZ) basis set (Dunning 1989). The experimental and calculated infrared intensities and vibrational frequencies used to calculate the D₂O and D₂O₂ infrared signatures within an O₂ matrix are presented in Tables 4 and 5, respectively.

In the case of the radical species DO₂ and OD, it was necessary to calculate infrared intensities that would be utilized directly toward quantitative analysis. In such cases, for greater

Table 6

Compiled Experimental and Calculated Values for the Vibrational Frequencies and Intensities of the Hydroxyl Radical (OH), and Its Deuterated Counterpart (OD)

Mode	Experimental Values				Calculated Values								Best Estimated Value	
	OH _(g) ^a		OH _(s) ^b		OH ^c		OH ^a		OD ^c		OD, PCM ($\Sigma = 1.5$) ^c		OD _(O2)	
	Freq, cm ⁻¹	A Value, cm molecule ⁻¹	Freq, cm ⁻¹	A Value, cm molecule ⁻¹	Freq, cm ⁻¹	A Value, cm molecule ⁻¹	Freq, cm ⁻¹	A Value, cm molecule ⁻¹	Freq, cm ⁻¹	A Value, cm molecule ⁻¹	Freq, cm ⁻¹	A Value, cm molecule ⁻¹	Freq, cm ⁻¹	A Value, cm molecule ⁻¹
ν_1	<i>3570</i>	<i>1.0 × 10⁻¹⁸</i>	3549	3547	1.6 × 10 ⁻¹⁸	<i>3576</i>	<i>1.6 × 10⁻¹⁸</i>	2611	8.8 × 10 ⁻¹⁹	2609	1.5 × 10 ⁻¹⁸	2612	1.5 × 10 ⁻¹⁸	

Notes. Best estimate frequency and intensity values are also listed; calculated via the scheme described in the text. Italicized values were not used in the best estimate calculations and are given for comparison only.

^a Taken from Lane & Kjaergaard (2010). Calculated values are CCSD(T)-F12/cc-pVQZ-F12 (anharmonic).

^b Langford et al. (2000) isolated within an Ar matrix.

^c B3LYP/cc-pVQZ (anharmonic).

Table 7Compiled Experimental and Calculated Values for the Vibrational Frequencies and Intensities of the Hydroperoxy Radical (HO₂) and Its Deuterated Counterpart (DO₂)

Mode	Experimental Values				Calculated Values								Best Estimated Value	
	HO _{2(g)}		HO _{2(O2)} ^a DO _{2(O2)} ^a		DO ₂ ^b		DO ₂ ^c		DO ₂ , PCM ($\Sigma = 1.5$) ^c		DO _{2(O2)}			
	Freq, cm ^{-1d}	A Value, cm molecule ^{-1d}	A Value, cm molecule ^{-1e}	Freq, cm ⁻¹	Freq, cm ⁻¹	Freq, cm ⁻¹	A Value, cm molecule ⁻¹	Freq, cm ⁻¹	A Value, cm molecule ⁻¹	Freq, cm ⁻¹	A Value, cm molecule ⁻¹	Freq, cm ⁻¹	A Value, cm molecule ⁻¹	
ν_1	<i>3436</i>	<i>8.1 × 10⁻¹⁹</i>	...	<i>3400</i>	<i>2521</i>	2582	4.7 × 10 ⁻¹⁸	2625	2.1 × 10 ⁻¹⁸	2628	3.3 × 10 ⁻¹⁸	2585	7.4 × 10 ⁻¹⁸	
ν_2	<i>1392</i>	<i>2.4 × 10⁻¹⁸</i>	...	<i>1392</i>	<i>1024</i>	1060	7.9 × 10 ⁻¹⁸	1053	5.6 × 10 ⁻¹⁸	1059	6.4 × 10 ⁻¹⁸	1066	9.1 × 10 ⁻¹⁸	
ν_3	<i>1098</i>	<i>1.4 × 10⁻¹⁸</i>	3.6 × 10 ⁻¹⁸	<i>1101</i>	<i>1123</i>	1137	1.5 × 10 ⁻¹⁸	1180	1.3 × 10 ⁻¹⁸	1184	1.5 × 10 ⁻¹⁸	1141	1.7 × 10 ⁻¹⁸	

Notes. Best estimate frequency and intensity values are also listed; calculated via the scheme described in the text. Italicized values were not used in the best estimate calculations and are given for comparison only.

^a Taken from Tso & Lee (1985) in a solid O₂ matrix.

^b CCSD(2)_T/cc-pVTZ (anharmonic). Estimated values are based on these calculations for reasons discussed in the text.

^c B3LYP/cc-pVQZ (harmonic).

^d Taken from Zahniser et al. (1989).

^e Taken from Sakamoto & Tonokura (2012). Intensities of HO₂ are presented, calculated at several different levels of theory.

Table 8Compiled Experimental and Calculated Values for the Vibrational Frequencies and Intensities of Ozone (O₃), Extended to Include Several Combination Bands

Mode	Experimental Values				Calculated Values								Best Estimated Value	
	O _{3(g)} ^a		O _{3(s)} ^b		O ₃ ^c		O ₃ ^d		O ₃ , PCM ($\Sigma = 1.5$) ^d		O _{3(O2)}			
	Freq, cm ⁻¹	A Value, cm molecule ⁻¹	Freq, cm ⁻¹	A Value, cm molecule ⁻¹	Freq, cm ⁻¹	A Value, cm molecule ⁻¹	Freq, cm ⁻¹	A Value, cm molecule ⁻¹	Freq, cm ⁻¹	A Value, cm molecule ⁻¹	Freq, cm ⁻¹	A Value, cm molecule ⁻¹		
ν_1	1103	1.8 × 10 ⁻¹⁹	<i>1231</i>	5.6 × 10 ⁻²⁰	1152	1.7 × 10 ⁻²⁰	1157	3.3 × 10 ⁻²⁰	1108	2.7 × 10 ⁻¹⁹		
ν_2	701	7.1 × 10 ⁻¹⁹	<i>735</i>	1.7 × 10 ⁻¹⁸	699	1.1 × 10 ⁻¹⁸	700	1.2 × 10 ⁻¹⁸	702	8.0 × 10 ⁻¹⁹		
ν_3	1042	1.5 × 10 ⁻¹⁷	1050 ± 11	3.6 × 10 ⁻¹⁸	<i>1171</i>	3.1 × 10 ⁻¹⁷	1014	3.5 × 10 ⁻¹⁷	1006	4.3 × 10 ⁻¹⁷	1034	1.9 × 10 ⁻¹⁷		
$\nu_1 + \nu_2$	1795	1.7 × 10 ⁻²⁰	<i>1969</i>	1.8 × 10 ⁻²⁰	1856	1.7 × 10 ⁻²⁰	1864	1.7 × 10 ⁻²⁰	1803	1.7 × 10 ⁻²⁰		
$\nu_1 + \nu_3$	2111	1.3 × 10 ⁻¹⁸	2110 ± 5	4.6 × 10 ⁻¹⁹	<i>2383</i>	2.0 × 10 ⁻¹⁸	2141	2.4 × 10 ⁻¹⁸	2142	2.9 × 10 ⁻¹⁸	2112	1.5 × 10 ⁻¹⁸		
$\nu_2 + \nu_3$	1727	6.6 × 10 ⁻²⁰	<i>1894</i>	1.3 × 10 ⁻¹⁹	1698	2.7 × 10 ⁻¹⁹	1690	3.0 × 10 ⁻¹⁹	1719	6.6 × 10 ⁻²⁰		

Notes. Best estimate frequency and intensity values are also listed; calculated via the scheme described in the text. Italicized values were not used in the best estimate calculations and are given for comparison only.

^a Taken from Adler-Golden et al. (1985).

^b Taken from Raut et al. (2011).

^c B3LYP/6-311+G* (anharmonic, 2-mode coupling).

^d PBE/6-311+G* (anharmonic, 2-mode coupling).

accuracy, the anharmonic potential energy surface was explicitly calculated using the VSCF method without mode coupling (Chaban et al. 1999). For OD, the B3LYP/cc-pVQZ results were in good agreement with both the experimentally determined values as well as the high-level CCSD(T)-F12/cc-pVQZ-F12 calculations of Lane & Kjaergaard (2010), indicating that this level of theory was sufficient. However, for DO₂, it was hard to determine whether the B3LYP/cc-pVQZ method was reli-

able since discrepancies were found in the literature regarding both experimental and theoretical values for this species, or its hydrogenated counterpart (Zahniser et al. 1989; Sakamoto & Tonokura 2012). Therefore, the high-level coupled-cluster singles and doubles with a second-order perturbation correction in the space of triples (CCSD(2)_T) level of theory was used for this species. Here, CCSD(2)_T has been demonstrated to be capable of accurately reproducing potential energy surfaces at

large interatomic distances (important for anharmonic calculations), as well as being proficient in dealing with difficult cases such as biradicals, bond-breaking and treating large non-dynamical correlation effects (Gwaltney & Head-Gordon 2001; Piecuch et al. 2002; Piecuch & Wloch 2005; Keçeli et al. 2009). Since anharmonic calculations at this level of theory are computationally demanding, the reduced basis set of triple-zeta quality (cc-pVTZ) was used here. The experimental and calculated infrared intensities and vibrational frequencies used to calculate the OD and DO₂ infrared signatures within an O₂ matrix are presented in Tables 6 and 7, respectively.

The case of O₃ is also particularly challenging, since its ground state has considerable multireference character and is notoriously difficult to treat even with traditional high-level theoretical approaches (e.g., Jalbout 2002; Hino et al. 2006). In addition, anharmonic calculations were also necessary since—in the case of O₃—we are interested in the intensities of the combination bands, which require two-mode coupling to be calculated (i.e. 816 single point calculations for each potential energy surface). The B3LYP method poorly describes the potential energy surface of O₃, yet, since the use of coupled-cluster methods with solvation methods is not currently implemented in the GAMESS(US) package, a different DFT functional is required. The PBE functional was found to give a more satisfactory description of the O₃ potential energy surface (Perdew et al. 1996). For O₃, a smaller extended pople-style basis set of triple-zeta quality augmented with a diffuse polarization function (6–311+G*) was used to conserve computational resources during the anharmonic PCM calculations (Krishnan et al. 1980). The experimental and calculated infrared intensities and vibrational frequencies used to calculate O₃ infrared signatures within an O₂ matrix are presented in Table 8.

REFERENCES

- Adler-Golden, S. M., Langhoff, S. R., Bauschlicher, C. W., Jr., & Carney, G. S. 1985, *JChPh*, **83**, 255
- Aragones, J. L., MacDowell, L. G., & Vega, C. 2011, *JPCA*, **115**, 5745
- Ayouz, M., & Babikov, D. 2013, *JChPh*, **138**, 164311
- Becke, A. D. 1993, *JChPh*, **98**, 5648
- Bennett, C. J., Jamieson, C., Mebel, A. M., & Kaiser, R. I. 2004, *PCCP*, **6**, 735
- Bennett, C. J., & Kaiser, R. I. 2005, *ApJ*, **635**, 1362
- Bergin, E. A., Melnick, G. J., Stauffer, J. R., et al. 2000, *ApJL*, **539**, L129
- Bergman, P., Parise, B., Liseau, R., et al. 2011, *A&A*, **531**, L8
- Bergren, M. S., Schuh, D., Sceats, M. G., & Rice, S. A. 1978, *JChPh*, **69**, 3477
- Bertie, J. E., & Whalley, E. 1964, *JChPh*, **40**, 1637
- Boogert, A. C. A., Pontoppidan, K. M., Knez, C., et al. 2008, *ApJ*, **678**, 985
- Brewer, L., & Wang, L.-F. 1972, *JChPh*, **36**, 759
- Ceponkus, J., & Nelander, B. 2004, *JPCA*, **108**, 6499
- Chaban, G. M., Jung, J. O., & Gerber, R. B. 1999, *JChPh*, **111**, 1823
- Cheung, A. C., Thornton, D. D., Rank, D. M., Welch, W. J., & Townes, C. H. 1969, *Natur*, **221**, 626
- Cooper, P. D., Moore, M. H., & Hudson, R. L. 2006, *JPCA*, **110**, 7985
- Cuppen, H. M., & Herbst, E. 2007, *ApJ*, **668**, 294
- Cuppen, H. M., Ioppolo, S., Romanzin, C., & Linnartz, H. 2010, *PCCP*, **12**, 12077
- Dawes, R., Lolur, P., Ma, J., & Guo, H. J. 2011, *JChPh*, **135**, 081102
- Dozova, N., Krim, L., Alkikhani, M. E., & Lacombe, N. 2006, *JPCA*, **110**, 11617
- Du, F., Parise, B., & Bergman, P. 2012, *A&A*, **538**, A91
- Dulieu, F., Amiaud, L., Congiu, E., et al. 2010, *A&A*, **512**, A30
- Dunning, T. H. 1989, *JChPh*, **90**, 1007
- Ehrenfreund, P., Boogert, A. C. A., Gerakines, P. A., Tielens, A. G. G. M., & van Dishoeck, E. F. 1997, *A&A*, **328**, 649
- Ellingson, B. A., Theis, D. P., Tishchenko, O., Zheng, J., & Truhlar, D. G. 2007, *JPCA*, **111**, 13554
- Engdahl, A., & Nelander, B. 2004, *PCCP*, **6**, 730
- Ennis, C. P., Bennett, C. J., & Kaiser, R. I. 2011, *PCCP*, **13**, 9469
- Fernández-Ramos, A., & Varandas, A. J. C. 2002, *JPCA*, **106**, 4077
- Frenklach, M. 1984, *CoFl*, **58**, 69
- Frenklach, M., Packard, A., & Feeley, R. 2007, in *Modeling of Chemical Reactions*, ed. R. W. Carr (Elsevier Series Comprehensive Chemical Kinetics, Vol. 42; Amsterdam: Elsevier), 243
- Frenklach, M., Wang, H., & Rabinowitz, M. J. 1992, *PrECS*, **18**, 47
- Fulvio, D., Sivaraman, B., Baratta, G. A., Palumbo, M. E., & Mason, N. J. 2009, *AcSpA*, **72**, 1007
- Galabov, B., Yamaguchi, Y., Remington, R. B., & Schaeffer, H. F., III. 2002, *JPCA*, **106**, 819
- Ge, Y., Oslen, K., Kaiser, R. I., & Head, J. D. 2006, in *AIP Conf. Proc.* 855, *Astrochemistry: From Laboratory Studies to Astronomical Observations*, ed. R. I. Kaiser, P. Bernath, Y. Osamura, S. Petrie, & A. M. Mebel (Melville, NY: AIP), 253
- Gerakines, P. A., Schutte, W. A., Greenberg, J. M., & van Dishoeck, E. F. 1995, *A&A*, **296**, 810
- Gibb, E. L., Whittet, D. C. B., Boogert, A. C. A., & Tielens, A. G. G. M. 2004, *ApJS*, **151**, 35
- Gillett, F. C., & Forrest, W. J. 1973, *ApJ*, **179**, 483
- Ginovska, B., Camaioni, D. M., & Dupuis, M. 2007, *JChPh*, **127**, 084309
- Goldsmith, P. F., Liseau, R., Bell, T. A., et al. 2011, *ApJ*, **737**, 96
- Gordon, M. S., & Schmidt, M. W. 2005, in *Theory and Applications of Computational Chemistry: The first forty years*, ed. C. E. Dykstra, G. Frenking, K. S. Kim, & G. E. Scuseria (Amsterdam: Elsevier)
- Gwaltney, S. R., & Head-Gordon, M. 2001, *JChPh*, **115**, 2014
- Hasegawa, T. I., Herbst, E., & Leung, C. M. 1992, *ApJS*, **82**, 167
- Hino, O., Kinoshita, T., Chan, G. K.-L., & Bartlett, R. J. 2006, *JChPh*, **124**, 114311
- Hudgins, D. M., Sandford, S. A., Allamandola, L. J., & Tielens, A. G. G. M. 1993, *ApJS*, **86**, 713
- Ioppolo, S., Cuppen, H. M., Romanzin, C., van Dishoeck, E. F., & Linnartz, H. 2008, *ApJ*, **686**, 1474
- Ioppolo, S., Cuppen, H. M., Romanzin, C., van Dishoeck, E. F., & Linnartz, H. 2010, *PCCP*, **12**, 12065
- Jalbout, A. F. 2002, *JMoSt*, **617**, 5
- Jing, D., He, J., Brucato, J., et al. 2011, *ApJL*, **741**, L9
- Johnson, T. J., Sams, R. L., Burton, S. D., & Blake, T. A. 2009, *Anal. Bioanal. Chem.*, **395**, 377
- Kaiser, R. I. 2002, *Chem. Rev.*, **102**, 1309
- Kaiser, R. I., Eich, G., Gabrysch, A., & Roessler, K. 1999, *A&A*, **346**, 340
- Kaiser, R. I., Eich, G., Gabrysch, A., & Roessler, K. 1997, *ApJ*, **484**, 487
- Keçeli, M., Shiozaki, T., Yagi, K., & Hirata, S. 2009, *MolPh*, **107**, 1283
- Krishnan, R., Binkley, J. S., Seeger, R., & Pople, J. A. 1980, *JChPh*, **72**, 650
- Lane, J. R., & Kjaergaard, H. G. 2010, *JChPh*, **132**, 174304
- Langford, V. S., McKingley, A. J., & Quickenden, T. I. 2000, *JChS*, **122**, 12859
- Larsson, B., Liseau, R., Pagani, L., et al. 2007, *A&A*, **466**, 999
- Lee, C., Yang, W., & Parr, R. G. 1988, *PhRvB*, **37**, 785
- Leopold, N., Bushe, S., Gauglitz, G., & Lendl, B. 2009, *AcSpA*, **72**, 994
- Li, A., Xie, D., Dawes, R., et al. 2010, *JChPh*, **133**, 144306
- Liseau, R., Goldsmith, P. F., Larsson, B., et al. 2012, *A&A*, **541**, A73
- Loeffler, M. J., Raut, U., Vidal, R. A., Baragiola, R. A., & Carlson, R. W. 2006, *Icar*, **180**, 265
- Miyauchi, N., Hidaka, H., Chigai, T., et al. 2008, *CPL*, **456**, 27
- Mokrane, H., Chaabouni, H., Accolla, M., et al. 2009, *ApJL*, **705**, L195
- Moravej, M., Yang, X., Hicks, R. F., Penelon, J., & Babayan, S. E. 2006, *JAP*, **99**, 093305
- Oba, Y., Moyauchi, N., Hidaka, H., et al. 2009, *ApJ*, **701**, 464
- Oba, Y., Watanabe, N., Hama, T., et al. 2012, *ApJ*, **749**, 67
- Okabe, H. 1978, *Photochemistry of Small Molecules* (New York: Wiley)
- Parise, B., Bergman, P., & Du, F. 2012, *A&A*, **541**, L11
- Perdew, J. P., Burke, K., & Ernzerhof, M. 1996, *PhRVL*, **77**, 3865
- Piecuch, P., Kucharski, S. A., Kowalski, K., & Musial, M. 2002, *CoPhC*, **149**, 71
- Piecuch, P., & Wloch, M. 2005, *JChPh*, **123**, 224105
- Pilla, S., Hamida, A., Muttalib, K. A., & Sullivan, N. S. 2008, *PhRvB*, **77**, 224108
- Raut, U., Loeffler, M. J., Famá, M., & Baragiola, R. A. 2011, *JChPh*, **134**, 194501
- Roberts, H., & Herbst, E. 2002, *A&A*, **395**, 233
- Romanzin, C., Ioppolo, S., Cuppen, H. M., van Dishoeck, E. F., & Linnartz, H. 2011, *JChPh*, **134**, 084504
- Sakamoto, Y., & Tonokura, K. 2012, *JPCA*, **116**, 215
- Schmidt, M. W., Baldrige, K. K., Boatz, J. A., et al. 1993, *JCoCh*, **14**, 1347
- Seidler, P., Kongsted, J., & Christainsen, O. 2007, *JPCA*, **111**, 11205
- Silveira, D. M., Caridade, P. J. S. B., & Varandas, A. J. C. 2004, *JPCA*, **108**, 8721
- Smith, R. G., Charnley, S. B., Pendleton, Y. J., et al. 2011, *ApJ*, **743**, 131

- Stephan, K., Helm, H., & Märk, T. D. 1980, JChPh, [73, 3763](#)
- Stephens, P. J., Devlin, F. J., Chabalowski, C. F., & Frisch, M. J. 1994, JPhCh, 88, 11623
- Tielens, A. G. G. M., & Hagen, W. 1982, A&A, [114, 245](#)
- Tomasi, J., Mennucci, B., & Cammi, R. 2005, [Chem. Rev.](#), 105, 2999
- Tso, T.-L., & Lee, E. K. C. 1985, JPhCh, 89, 1618
- Vandenbussche, B., Ehrenfreund, P., Boogert, A. C. A., et al. 1999, A&A, [346, L57](#)
- Wang, Y., & Bowman, J. M. 2011, JChPh, [134, 154510](#)
- Zahniser, M. S., McCurdy, K. E., & Stanton, A. C. 1989, JPhCh, 93, 1065
- Zheng, W., Jewitt, D., & Kaiser, R. I. 2007, [CPL](#), [435, 289](#)
- Ziegler, J. D. 1999, JAP, [85, 1249](#)